A novel two-level approach to defect detection in braided CFRP using Air-coupled ultrasonic testing

Chenchen Zhang [1], *Yinghong Zhang* [2], *Dianzi Liu* [3*], *Xiaojia Zhang* [4], *Xianwei Wu* [1], *Zhenghua Qian* [1,*], *Xiangyu Li* [5]

[1] *State Key Laboratory of Mechanics and Control of Mechanical Structures, College of Aerospace Engineering, Nanjing University of Aeronautics and Astronautics, Nanjing 210016, China*

[2] *School of Mechanical and Electrical Engineering, Guilin University of Electronic Technology, Guilin 541004, China*

[3] *School of Engineering, University of East Anglia, Norwich NR4 7TJ, UK*

[4] *CNPC Tubular Goods Research Institute，Xi'an, 710077,China*

[5] *Applied Mechanics and Structure Safety Key Laboratory of Sichuan Province, School of Mechanics and Engineering, Southwest Jiaotong University, Chengdu 610031, China*

[*] *Corresponding author.*

E-mail addresses: dianzi.liu@uea.ac.uk (*Dianzi Liu*), *qianzh@nuaa.edu.cn* (*Zhenghua Qian*).

ABSTRACT： Air-coupled ultrasonic testing and C-scan technique has been increasingly applied to the braided CFRP structures owing to its non-destruction, non-contact and high visualization characteristics. Due to the noise, structural vibration, and airflow in the process of detection, the accuracy of defect identification is easily deteriorated. To address this issue and further determine the relationship between the ultrasonic acoustical pressure attenuation and structural parameters, a novel two-level identification method based on the modified two-dimensional variational mode decomposition (2D-VMD) has been proposed. In the first level, C-scan images have been sparsely decomposed into ensembles of modes by 2D-VMD method. Then, the modes have been screened by

mutual information method to realize the reconstruction of new image in the second level. Experimental results have shown that the proposed method has the good ability to identify defects with a minimum detectable diameter of 1~2mm. It has been noted that the ultrasonic acoustical pressure attenuation has become remarkably higher in the twill weave CFRP than the plain weave CFRP and the ratio of pressure attenuation between two weave types of CFRP has decreased with the defect depth increase. Meanwhile, shadows around defects in C-scan images have been suppressed to a great extent. It has been demonstrated that the capability of denoising has enabled the developed method with the accurate detection in terms of the shape, size, depth and weave type. With these advantages, the proposed method has provided valuable insights into the development of an effective method for defect detection of braided CFRP structures.

Keywords：Air-coupled ultrasonic testing; Braided CFRP; Two-Dimensional Variational Mode Decomposition; Defect identification

1. Introduction

CFRP structures have been widely used in engineering sectors, such as automotive, aerospace, energy and marine industries due to their extra high strength-to-weight and stiffness-to-weight ratios. However, the micro defects including voids, cracks, delamination and inclusions usually lead to the performance degradation of braided CFRP structures. Thus, the demand for developing efficient and effective defect detection techniques with the ability to the quality assessment of CFRP structures is becoming increasingly serious. For contact detection techniques, a relatively flat surface is required to achieve the efficient acoustical coupling during the test process. As the wrap texture of braided CFRP is irregular in general which leads to the reduction of the transferred acoustical energy. To address this issue, the Air-coupled ultrasonic testing (ACUT) technique gradually comes into public

attention due to its no need for coupling medium and non-contact characteristics, especially in the detection of composite structures.

In 2003, the combination of the transmission with the guided wave methods was adopted to assist ACUT for the detection of the flaws, damages and normal inter defects in CFRP composites[1]. Also, ACUT was employed to measure and evaluate the fiber orientations in orthotropic composite laminates[2]. As compared with the quality of detecting GFRP(Glass Fiber Reinforced Polymer), ACUT in CFRP has better results of detection in terms of the shape, magnitude, thickness and position[3].The abilities of ACUT and AIRT (active infrared thermography) to detect the delamination of GFRP composites were compared both qualitatively and quantitatively[4]. Osama Ahmed[5] compared different non-destructive testing and evaluation methods for selecting the most suitable technique in the detection of fiber-reinforced polymer composites. ACUT is utilized to excite multiple Lamb waves in polymer plates, and the results prove that the conversion from A0 mode to S0 mode can be used for defect detection[6]. M.S. Harb [7]shows the ability of A0 mode for the identification of delamination in composite laminate. The through-transmission ultrasonic acoustography demonstrated a good result in the detection of foreign object inclusion in graphite epoxy composites[8]. Jeong H [9] observed that when the porosity of CFRP kept consistent, the attenuation curves of CFRP laminates showed approximately linear behaviors with the frequency. As compared with the cured CFRP laminate[10], the uncured CFRP laminate had the property with the more severe ultrasonic energy attenuation. Biwa[11] also provided an formulation for the attenuation coefficients of the plane wave propagating in composite in terms of the scattering, the absorption cross-sections of a single inclusion and the attenuation properties of the matrix. However, the theoretical results of attenuation coefficients only agreed with measurements at low porosity or

frequency, owing to the important reason of neglecting the randomness and complexity of real voids. Although Ding[12] established a real morphology void model to verify the non-unique corresponding relationship between the porosity and ultrasonic energy attenuation coefficient, it has been a challenging problem to accurately calculate the attenuation coefficients using analytical methods for composite materials.

The C-scan technique plays an important role in ACUT owing to its advantages of visualization and convenience. Tian[13,14]investigated the delamination defects which were induced by impacts and obtained the results including the size and shape using ultrasonic C-scan images. Also, it was noted that the resonance frequency of the excitation had an influence on the damage detection of multi-layer, multi-material composites in ACUT resonance imaging[15]. Asokkumar et al [16] utilized highly focused transducers to obtain high resolution topography images of structural polymer surfaces. The results of C-scan showed a good detectability, but the time-consuming process in the test[17]. Even the C-scan technique has the ability to identify the size and shape of impact-type defect, it comes with the necessity of access to both sides of the specimen, leading to a higher demand for the test environment. Leslie Bustamante [18] realized the defect identification of aluminum, CFRP and epoxy-resin specimens, then constructed the 2D images. On that basis, the size and location of artificial defects were detected and identified through the changes in B-scan amplitudes of Lamb waves propagated in CFRP[19].

In actual ACUT circumstance, the large acoustic impedance mismatch at the air-solid interface reduces the efficiency of ultrasound energy transfer, resulting in a lower SNR of the received signal and the transmission initial wave will not be recognized precisely[20]. In order to eliminate the noise of two-dimensional images in ACUT, some signal processing methods have been applied to improve

the accuracy of defect detection in CFRP composites. For example, the empirical mode decomposition (EMD) method was originally proposed for 1D signal and then extended to deal with two-dimensional images by Huang[21]. This method decomposed the nonlinear and non-stationary signals into a series of intrinsic mode functions (IMFs) containing definite physical meanings and instantaneous features. Chang [22] utilized the pulsed thermography (PT) technique to visualize the defects inside CFRP specimens. Combining the multi-dimensional ensemble empirical mode decomposition (MEEMD) technique, the noise and the non-uniform backgrounds in thermal images can be removed from the thermographic data. However, the limitations including the sensitivity to noise and the lack of the mathematical theory definitely restrained EMD-based methods from their wide applications. Taking into account the above issues, a mode decomposition method, called variational mode decomposition (VMD) [23], has been proposed. As a non-recursive decomposition method, VMD takes advantage of the EMD method and simultaneously achieves a finite number of band limited IMFs. With the implementation of Wiener filtering to update the modes directly in the Fourier domain[24], VMD is less sensitive to noise as compared with the EMD based methods. Two-dimensional variational mode decomposition (2D-VMD)[25], an image process method, has the ability to adaptively decompose an image into a few different modes of separate spectral bands with specific directional and oscillatory characteristics. However, there is still no completely non-contact and high-precision defect identification technique to evaluate the size, shape and depth of defects in CFRP structures.

In this work, a novel two-level identification method based on 2D-VMD has been proposed in this paper to assess artificial defects and the attenuation of ultrasonic waves which propagate through braided CFRP structures using ACUT technique. At the first level, images produced by C-

scan have been utilized to evaluate the details of damage in ACUT. As the acoustical pressure of ultrasonic transmission waves has been already attenuated after ultrasonic wave passing through detection points, the pixel in C-scan image has been further processed using 2D-VMD method to deal with noise, structural vibration and other influences in the process of C-scan. Then, the sifting of modes and reconstruction of new images have been realized at the second level. By extracting the damaged information in reconstructed image, the relationships among ultrasonic acoustical pressure attenuation, the depth of defects and the weave type of carbon fibers have been established to achieve the non-contact, high-precision defect detection and identification in braided CFRP structures.

2. Two-level methodology for defect detection in braided CFRP

2.1 Two-dimensional Variational Mode Decomposition

1D-VMD model is suitable for processing one-dimensional (A-scan) signals which contain multiple frequencies in the ultrasonic nondestructive testing. In ACUT, C-scan technique is often utilized to detect damages in different materials. The process of C-scan is accompanied by the generation of two-dimensional images, which consist of surface and internal damage information of detected structure. Each pixel value of C-scan images is taken from the peak value of ultrasonic direct wave at each detection point to construct the elements in the corresponding matrix for damage detection. The matrices can truly reflect the attenuation of ultrasonic acoustical pressure traversing through the detection area. Aiming at better handling C-scan images, 1D-VMD model has been extended in the two-dimensional level to process two-dimensional information with the same properties as one-dimensional analytic signal in frequency domain.

2.1.1 2D analytic signal

For 1D signals or 2D images, the single-sidedness of analytic signal spectrum represented by the negative half-plane of the frequency domain needs to be set to zero. Thus, the shifting frequencies of 2D analytic signals to the base-band by complex exponential mixing can be easily achieved.

In general, 2D analytic signal can be defined in the frequency domain:

$$\hat{u}_{AS,\xi}(\vec{\omega}) = \begin{cases} 2\hat{u}_{\xi}(\omega), \text{if} \quad \vec{\omega}\cdot\vec{\omega}_{\xi} > 0 \\ \hat{u}_{\xi}(\omega), \quad \text{if} \quad \vec{\omega}\cdot\vec{\omega}_{\xi} = 0 \\ 0, \quad \text{if} \quad \vec{\omega}\cdot\vec{\omega}_{\xi} < 0 \end{cases} = (1+\text{sgn}(\vec{\omega}\cdot\vec{\omega}_{\xi}))\hat{u}_{\xi}(\vec{\omega}) \tag{1}$$

The generalized 2D analytic signal with above-mentioned characteristics in the frequency domain can be reformulated as:

$$u_{AS,\xi}(\vec{x}) = u_{\xi}(\vec{x}) * \left(\delta(\langle \vec{x}, \vec{\omega}_{\xi} \rangle) + \frac{j}{\pi \langle \vec{x}, \vec{\omega}_{\xi} \rangle} \right) \delta(\langle \vec{x}, \vec{\omega}_{\xi}, \perp \rangle) \tag{2}$$

where $*$ denotes the convolution; ξ is the number of modes; $\hat{u}_{\xi}(\omega)$ represents the sub-signals in frequency domain; ω_{ξ} is the associated center frequency. The analytic signal is calculated line-wise along the reference direction- $\vec{\omega}_{\xi}$. δ is the Dirac distribution.

2.1.2 2D-VMD Functional

Each mode decomposed by 2D-VMD functional has its own center frequencies and bandwidths. The bandwidth of mode can be defined as the squared L^2-norm of the gradient of 2D analytic signal:

$$\left\| \nabla \left[u_{AS,\xi}(x) e^{-j\langle \omega_{\xi}, x \rangle} \right] \right\|_2^2 \tag{3}$$

Here, the squared norm can be understood as

$$\| \cdot \|_2^2 = \int_R | \cdot \ (x)|^2 dx \tag{4}$$

The objective function is to minimize the sum of bandwidths for all modes. Meanwhile, as the

sum of energy in all the modes after decomposition should be equal to what is represented in original analytic signal, therefore the variational function based on 2D analytic signal[26] can be formulated as:

$$\min_{u_\xi,\bar{\omega}_\xi}\left\{\sum_\xi\left\|\nabla\left[u_{AS,\xi}(\vec{x})e^{-j\langle\bar{\omega}_\xi,\vec{x}\rangle}\right]\right\|_2^2\right\} \qquad (5)$$
$$s.t. \qquad \forall x:\sum_\xi u_\xi(x)=\ell(x)$$

where $\ell(x)$ denotes the 2D input signal.

To improve the computational efficiency and increase the fidelity of the signal, a Lagrange multiplier and a quadratic penalty term are introduced to convert the variational function into a unconstrained optimization problem in the reconstruction procedure. The solution is obtained by ADMM (Alternating Direction Method of Multiplies) method, which overcomes the issue arising in some cases where the quadratic penalty term coefficients approach infinity. It is worth noting that such issue will cause the instability of the approximate objective function, leading to the difficulty of obtaining the exact solution ultimately.

First, the modified variational constraint function is written as:

$$\begin{aligned}L(\{u_\xi\},\{\omega_\xi\},\lambda)&=\sum_\xi\beta_\xi\left\|\nabla\left[u_{AS,\xi}(x)e^{-j\langle\omega_\xi,x\rangle}\right]\right\|_2^2+\left\|\ell(x)-\sum_\xi u_\xi(x)\right\|_2^2+\left\langle\lambda(x),\ell(x)-\sum_\xi u_\xi(x)\right\rangle \\ &=\sum_\xi\beta_\xi\left\|\nabla\left[u_{AS,\xi}(x)e^{-j\langle\omega_\xi,x\rangle}\right]\right\|_2^2+\left\|\ell(x)-\sum_\xi u_\xi(x)+\frac{\lambda(x)}{2}\right\|_2^2-\left\|\frac{\lambda(x)}{2}\right\|_2^2\end{aligned} \qquad (6)$$

where λ is the Lagrange multiplier and β_ξ represents the penalty factor for the data-fidelity constraint.

Thus, the optimization problem defined by Eq.5 is transformed into the minimization of the maximum augmented Lagrange function defined by Eq.7 for seeking the saddle point.

$$\min_{u_\xi,\omega_\xi}\max_\lambda L(\{u_\xi\},\{\omega_\xi\},\lambda) \qquad (7)$$

Using ADMM, u_ξ and ω_ξ are updated as follows:

$$u_\xi^{n+1} = \arg\min_{u_\xi}\left\{\beta_\xi\left\|\nabla\left[u_{AS,\xi}(x)e^{-j\langle\omega_\xi,x\rangle}\right]\right\|_2^2 + \left\|\ell(x) - \sum_i u_i(x) + \frac{\lambda(x)}{2}\right\|_2^2\right\} \tag{8}$$

$$\omega_\xi^{n+1} = \arg\min_{\omega_\xi}\left\{\beta_\xi\left\|\nabla\left[u_{AS,\xi}(x)e^{-j\langle\omega_\xi,x\rangle}\right]\right\|_2^2\right\} \tag{9}$$

To obtain the solution to Eq.8, the variational function can be written in Fourier domain utilizing the Fourier isometry on L^2-norm:

$$\begin{aligned} u_\xi^{n+1} &= \arg\min_{u_\xi}\left\{\beta_\xi\left\|\mathrm{j}\omega\left[\hat{u}_{AS,\xi}(\omega+\omega_\xi)\right]\right\|_2^2 + \left\|\hat{\ell}(\omega) - \sum_i \hat{u}_i(\omega) + \frac{\hat{\lambda}(\omega)}{2}\right\|_2^2\right\} \\ &= \arg\min_{u_\xi}\left\{\beta_\xi\left\|\mathrm{j}(\omega-\omega_\xi)\hat{u}_{AS,\xi}(\omega)\right\|_2^2 + \left\|\hat{\ell}(\omega) - \sum_i \hat{u}_i(\omega) + \frac{\hat{\lambda}(\omega)}{2}\right\|_2^2\right\} \end{aligned} \tag{10}$$

Therefore, the frequency is shifted to the base-band through multiplying the analytic signal with a pure exponential function. Taking the first differentiation w.r.t $\hat{u}_\xi$ and setting it to 0, one has

$$2\beta_\xi\left|\omega-\omega_\xi\right|^2\hat{u}_\xi + (-1)\left(\hat{\ell}(\omega) - \sum_i \hat{u}_i(\omega) + \frac{\hat{\lambda}(\omega)}{2}\right) = 0 \qquad \text{s. t. } \forall\omega, \left\langle\omega, \omega_\xi\right\rangle \geq 0. \tag{11}$$

The mode is estimated by the solution of the optimized problem as follows:

$$\hat{u}_\xi^{n+1}(\omega) = \frac{\hat{\ell}(\omega) - \sum_{i\neq\xi}\hat{u}_i(\omega) + \frac{\hat{\lambda}(\omega)}{2}}{1 + 2\beta_\xi\left|\omega-\omega_\xi\right|^2} \tag{12}$$

where $\hat{\ell}(\omega)$, $\hat{u}_i(\omega)$, and $\hat{\lambda}(\omega)$ are the Fourier transforms of $\ell(x)$, $u(x)$, and $\lambda(x)$, respectively. n is the number of iterations.

Using Eqs.1 and 10, the central frequency ω_ξ as another solution of the variational function can be written in the frequency domain as:

$$\begin{aligned} \omega_\xi^{n+1} &= \arg\min_{\omega_\xi}\left\{\beta_\xi\left\|j(\omega-\omega_\xi)\left[\left(1+\mathrm{sgn}\left(\left\langle\omega_\xi,\omega\right\rangle\right)\right)\hat{u}_\xi(\omega)\right]\right\|_2^2\right\} \\ &= \arg\min_{\omega_\xi}\left\{4\beta_\xi\left\|(\omega-\omega_\xi)\hat{u}_\xi(\omega)\right\|_{\Omega_\xi}^2\right\} \end{aligned} \tag{13}$$

where Ω_ξ denotes the half-plane of the frequency domain.

The minimization can be achieved by a differential operation:

$$8\beta_\xi \int_{\Omega_\xi} \left(\omega-\omega_\xi\right)\left|\hat{u}_\xi\right|^2 d\omega = 0 \tag{14}$$

As the path of integration is on the half-plane Ω_ξ, the center frequency ω_ξ can be updated:

$$\omega_\xi^{n+1} = \frac{\int_{\Omega_\xi} \omega\left|\hat{u}_\xi^{n+1}(\omega)\right|^2 d\omega}{\int_{\Omega_\xi} \left|\hat{u}_\xi^{n+1}(\omega)\right|^2 d\omega} \tag{15}$$

The error between decomposed modes and the input signal can be represented by the equation $\hat{\ell}(\omega)-\sum_{i\neq\xi}\hat{u}_i(\omega)$. To reduce the error, the Lagrange multiplier λ is updated by a standard gradient ascent with the fixed time step τ using Eq 16:

$$\lambda^{n+1}(x) = \lambda^n(x) + \tau\left(\hat{\ell}(\omega)-\sum_{i\neq\xi}\hat{u}_i(\omega)\right) \tag{16}$$

Summarily, the flow chart for the procedure of 2D-VMD has been provided in **Fig.1**:

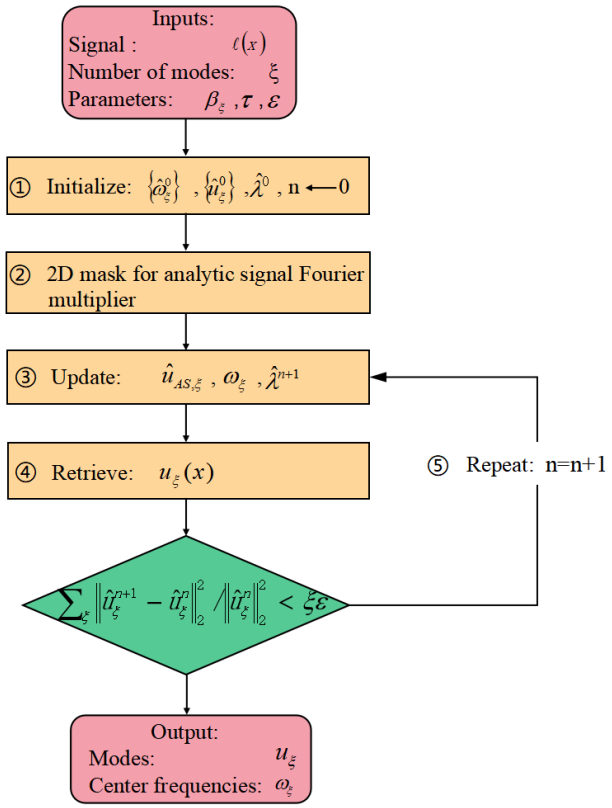

Fig.1 Flow chart of 2D-VMD method

2.2 Image reconstruction and the attenuation calculation of acoustical pressure

2.2.1 Mutual information (MI) method

The modes decomposed by 2D-VMD need to be screened for the reconstruction of a new image. Mutual information (MI) method shows the degree of the interdependence between two images. Therefore, this method i applied in this study to sift the modes for the reconstruction of new images, which have been analyzed to explore the relationship between the ultrasonic acoustical pressure attenuation and the defect depth in the second level.

The matrices **x** and **y** encompass information of defects from the original C-scan image (X**)** and the image represented by a decomposed mode (Y**)**, respectively. The joint probability density and marginal probability of two images have been defined as follows:

The joint probability density estimation:

$$\hat{p}(x,y)=\frac{1}{2\pi MN\sigma_1\sigma_2}\sum_{i=1}^{M}\sum_{j=1}^{N}e^{-\left[\frac{(x-x_{ij})^2}{2{\sigma_1}^2}+\frac{(y-y_{ij})^2}{2{\sigma_2}^2}\right]} \tag{17}$$

where M and N are the dimensions of **x** and **y**, respectively. σ_1 and σ_2 are the variances of a two-dimensional Gaussian kernel Function.

The marginal probability of two images:

$$p(x)=\sum_y \hat{p}(x,y) \tag{18}$$

$$p(y)=\sum_x \hat{p}(x,y) \tag{19}$$

Therefore, MI of the two images can be calculated using Eq. 20:

$$MI(X,Y)=\sum_{x,y}\hat{p}(x,y)\log_2\frac{\hat{p}(x,y)}{p(x)p(y)} \tag{20}$$

when $MI(X,Y)\geq\gamma$, where γ is the threshold value, the mode Y will be selected. Then, the next mode and the C-scan image X will be calculated using MI iteratively. It is noted that all the selected

modes have contributed to the reconstruction of the new image.

2.2.2 The attenuation of ultrasonic acoustical pressure in braided CFRP

The energy attenuation exists in the diffusion, absorption and scattering of ultrasonic waves propagating in some media. Energy attenuation in braided CFRP is easily influenced by many factors such as the frequency of excitation signal, the weave type, porosity and thickness of specimen. Ultrasonic energy attenuation further increases when defects like cracks, inclusions and stratification appear in the medium. This change of the energy attenuation in braided composite medium like CFRP or GFRP is non-linear and complicated, leading to the difficulty of calculation and defects identification. The overall performance of braided composites in the meso or microscopical level is usually equivalent to a single material behavior in a macroscopical level. Therefore, the braided CFRP specimens in the experimental tests are treated as a single medium to calculate the attenuation of the ultrasonic acoustical pressure.

The acoustical power is usually utilized to reveal the average energy density of acoustical waves and is also proportional to the square of the acoustical pressure. Thus, the energy attenuation of ultrasonic waves is proportional to the acoustical pressure attenuation. In the air, acoustical pressure attenuation is related to the frequency of excitation signal and the distance of propagation ,which is mathematically formulated by Eq.21：

$$\alpha(f) = \alpha_{air} f^2 L \tag{21}$$

where L is the propagation distance of ultrasonic in air; f represents the frequency of excitation signal and α_{air} denotes the attenuation coefficient, which is equal to 1.5985 $dB[MHz^2 \cdot cm]$.

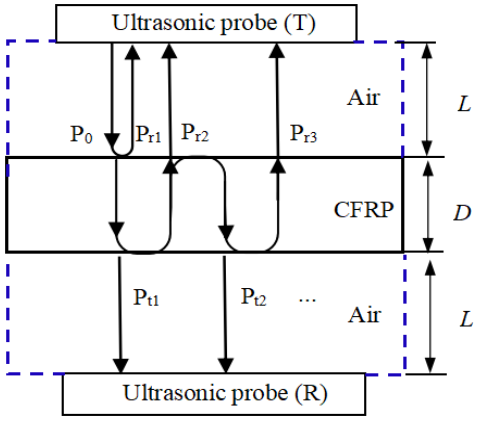

Fig.2 The propagation process of ultrasonic wave

The schematic diagram of the typical transmission process of ultrasonic waves between the air and braided CFRP is depicted in **Fig.2**. In the process of C-scan, the transducers are arranged on both sides of specimens, especially in a horizontal position and along the direction perpendicular to the specimen. Due to these arrangements, only the bulk wave excited by the transmitter propagates through the air into CFRP specimens then the transmission wave and multiple reflection waves are generated at the boundary. After the reflection, transmission and scattering in braided CFRP composites, the attenuated ultrasonic wave travels into the air until it is received by the other transducer.

The acoustical pressure at the propagation distance of a is assumed as $P = P_0 e^{j(\omega t - ka)}$, where P_0 denotes the acoustical pressure at the initial moment of ultrasonic propagation. Also, a is ranged from 0 to D and D is the thickness of braided CFRP specimens. The acoustical pressure of the first ultrasonic reflection wave is specified by Pr_1. Similarly, the acoustical pressure of the first ultrasonic transmission wave is defined as Pt_1. P_{rn} and P_{tn} (n=1, 2, 3…) represent acoustical pressures of the nth reflection and transmission waves, respectively. In the experiment, the values of L (the distance between the transducer and the specimen) and D are set to 38mm and 3.5mm.

The reflection and transmission of ultrasonic waves in braided CFRP specimens will be

generated between the pair of transducers until the energy is completely dissipated. k is the wave number of excitation signals and formulated by Eq.22:

$$k = \frac{2\pi}{\lambda} = \frac{2\pi f}{c} \tag{22}$$

where c denotes the velocity of ultrasonic longitudinal wave in materials. As the low density of braided CFRP composites is observed in the experiment, the velocity of the longitudinal wave propagated in the CFRP specimens is given as 3000m/s.

Thus, the total acoustical pressure of transmission waves at the distance of D can be calculated by

$$P_t = P_{t_1} + P_{t_2} + P_{t_3} + \cdots = \frac{P_0 t_1 t_2 e^{-jkD}}{1 - \frac{r_2}{r_1} e^{-j2kD}} \tag{23}$$

$$e^{-jkD} = \cos(kD) - j\sin(kD) \tag{24}$$

where t_1 and t_2 denote the ultrasonic transmission coefficients at the upper and lower surfaces of the braided CFRP specimen, respectively. r_1 and r_2 are the corresponding reflection coefficients.

Rewriting Eq.23, one has

$$P_t = \frac{P_0 t_1 t_2 (1 - \frac{r_2}{r_1})\cos(kD) - jP_0 t_1 t_2 (1 + \frac{r_2}{r_1})\sin(kD)}{(1 - \frac{r_2}{r_1})^2 \cos^2(kD) + (1 + \frac{r_2}{r_1})^2 \sin^2(kD)} \tag{25}$$

As the acoustical pressure in braided CFRP can be expressed in another way as $P = P_0 e^{j(wt-ka)} = A + jB$, the effective amplitude of the acoustical pressure is defined as

$$|P| = \sqrt{A^2 + B^2} \tag{26}$$

Similarly, the acoustical pressure of transmission waves superimposed at the lower boundary of braided CFRP specimen can be rewritten as

$$|P_t| = \frac{P_0 t_1 t_2}{\sqrt{(1-\frac{r_2}{r_1})^2 \cos^2(kD) + (1+\frac{r_2}{r_1})^2 \sin^2(kD)}} \tag{27}$$

Based on the ratio of the initial acoustical pressure to that of transmission waves, the total transmission coefficient of ultrasonic waves in braided CFRP can be formulated as

$$\begin{aligned} T = \frac{|P_t|}{|P_0|} &= \frac{t_1 t_2}{\sqrt{(1-\frac{r_2}{r_1})^2 \cos^2(kD) + (1+\frac{r_2}{r_1})^2 \sin^2(kD)}} \\ &= \frac{1}{\sqrt{\cos^2(\frac{2\pi}{\lambda}D) + \frac{1}{4}(R_{21}+R_{12})^2 \sin^2(\frac{2\pi}{\lambda}D)}} \end{aligned} \tag{28}$$

where $t_1 t_2 = \frac{4Z_1 Z_2}{(Z_1+Z_2)^2}$, $\frac{r_2}{r_1} = \left(\frac{Z_1 - Z_2}{Z_1 + Z_2}\right)^2$, $R_{12} = \frac{Z_2}{Z_1}$ and $R_{21} = \frac{Z_1}{Z_2}$. Z_1 and Z_2 are the acoustical impedance of the air and braided CFRP specimen, respectively.

The acoustic impedance of air (Z_1) and the specimen (Z_2) and the wavelength (λ) are all constant. Also, the transmittance of the acoustical pressure is a function of the specimen thickness. Under ideal circumstances, when $D = n\frac{\lambda}{2}$ $(n = 1,2,3\cdots)$, the thickness of CFRP specimen is an integer multiple of half-wavelengths. Therefore, the acoustical pressure transmission rate is approximately equal to 1, that is to say, the ultrasonic wave is nearly fully transmitted. Similarly, when $D = (2n\text{-}1)\frac{\lambda}{4}$ $(n = 1,2,3\cdots)$, the thickness is odd times of quarter-wavelengths and the transmittance is minimum.

The change of acoustical pressure amplitudes in decibels is defined as the acoustical pressure attenuation, which describes the change in ultrasonic energy of waves before and after transmitting into the test material. Taking the initial acoustical pressure as a reference, when a test specimen is placed between two transducers, the attenuation of the acoustical pressure in braided CFRP specimen can be expressed as

$$\alpha = 20\lg\frac{|P_0|}{|P_t|} = 20\lg\frac{1}{T} \tag{29}$$

In the ultrasonic non-destructive testing, the voltage amplitude of signals received by instrument is proportional to the acoustical pressure. Therefore, the ratio of the amplitude of received signals to the acoustical pressure is the same as the value at the different location and defined by

$$\frac{|P_t|}{|P_0|} = \frac{V_t}{V_0} \tag{30}$$

where V_t denotes the received signal amplitude and V_0 is the received signal amplitude of ultrasonic waves propagating across air.

Substituting Eq.30 into Eq.29, the attenuation of the ultrasonic acoustical pressure is written as:

$$\alpha = 20\lg\frac{V_0}{V_t} \tag{31}$$

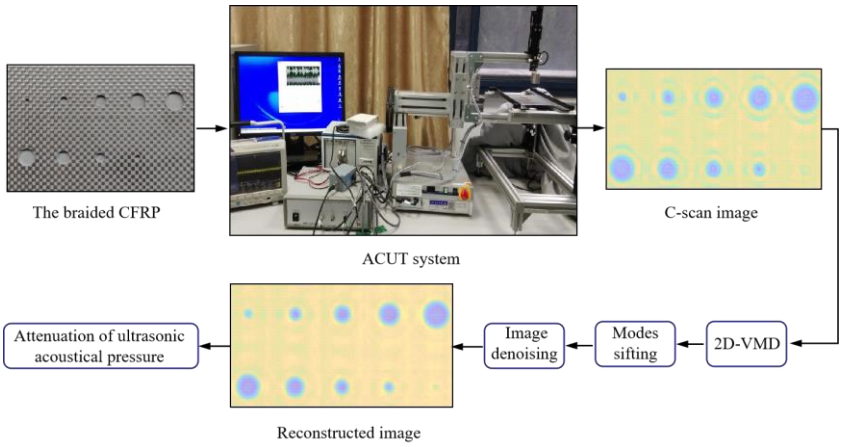

Fig. 3 Flowchart of the proposed two-level approach to defect detection

Based on the above descriptions of the developed two-level approach, the flowchart for the proposed methodology using 2D-VMD and MI for defects detection in braided CFRP has been given in **Fig. 3**.

3. Materials and experimental setup

3.1 The arrangement of braided CFRP specimens and artificial defects

Four braided CFRP specimens including three weave types of plain weave and one twill weave

in the experiments have the same size of 180mm×110mm×3.5mm. The plain weave CFRP has a higher stability, while the twill weave CFRP has less stress concentration when damaged and therefore it is more suitable for complex contour structural applications.

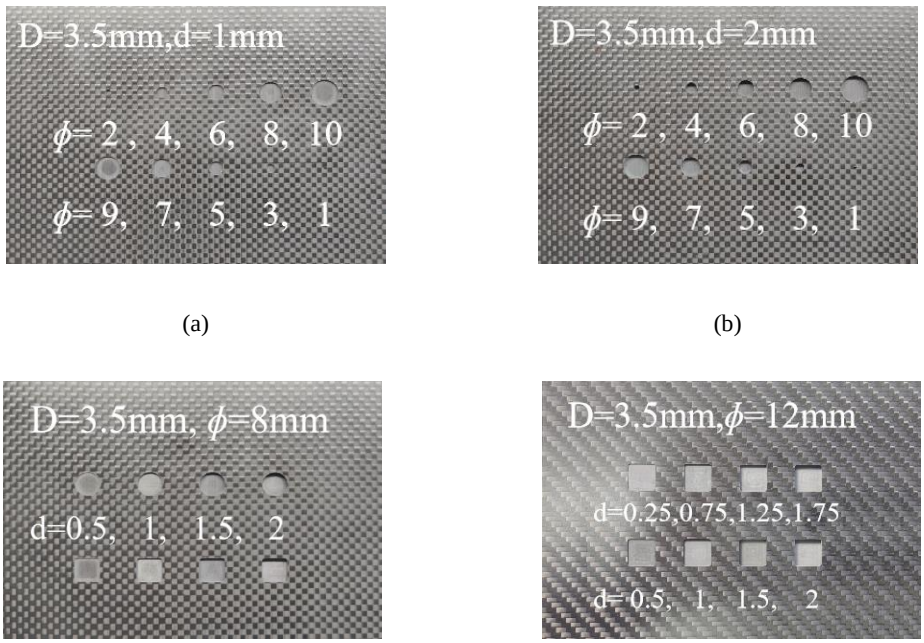

(a) (b)

(c) (d)

Fig.4 (a) Plain weave CFRP specimen with 1mm deep defects; **(b)** Plain weave CFRP specimen with 2mm deep defects; **(c)** Plain weave CFRP specimen with defects ranges from 0.5mm to 2mm in depth; **(d)** Twill weave CFRP specimen with defects ranges from 0.25mm to 2mm in depth;

Table 1 The details of CFRP specimens and defects

Cases	Weave type	Density(kg/m^3)	Artificial defects			
			Shape	Number	Diameter(mm)	Depth(mm)
a	Plain weave	1477.6	Circular	10	1~10	1.0
b	Plain weave	1477.6	Circular	10	1~10	2.0
c	Plain weave	1477.6	Circular & Square	8	8	0.5~2.0
d	Twill weave	1518.6	Square	8	12	0.25~2.0

Table 2 Performance parameters of typical braided CFRP

E_1(MPa)	E_2=E_3(MPa)	G_{12}=G_{13}(MPa)	G_{23}(MPa)	U_{12}=U_{13}	U_{23}
135000	8000	4500	2800	0.34	0.3

As shown in **Fig.4 (a)**, all artificial defects have the same depth of 1mm, the diameter of defects ranges from 1mm to 10mm. Secondly, the depth of artificial defects in **Fig.4 (b)** is 2mm and the diameter of defects is same as **Fig.4 (a)**. Then**,** the specimen in **Fig.4 (c)** has circular and square artificial defects, the depth of defects ranges from 0.5mm to 2mm. At the last, the twill weave CFRP specimen shown in **Fig.4 (d)**, the diameter of defects is 12mm and the depth ranges from 0.25mm to 2mm.

The detailed parameters of braided CFRP specimens and the defects are shown in **Table 1** and **Table 2**. The depth of artificial defects is defined as ***d***. ***E*** is elastic modulus, ***G*** is shear modulus, **U** is Poisson coefficient, the subscripts 1, 2 and 3 represent the fiber direction, vertical fiber direction and inter-layer direction, respectively.

3.2 Air-coupled ultrasonic testing system

As shown in **Fig.5**, ACUT system integrates a pair of point focused piezoelectric transducers with 38mm focal length and a valid region of 13mm of radius. This arrangement of transducers allows the bulk wave to propagate in CFRP specimen via transmission mode. The signal was received and digitized from JPR-600C machine.

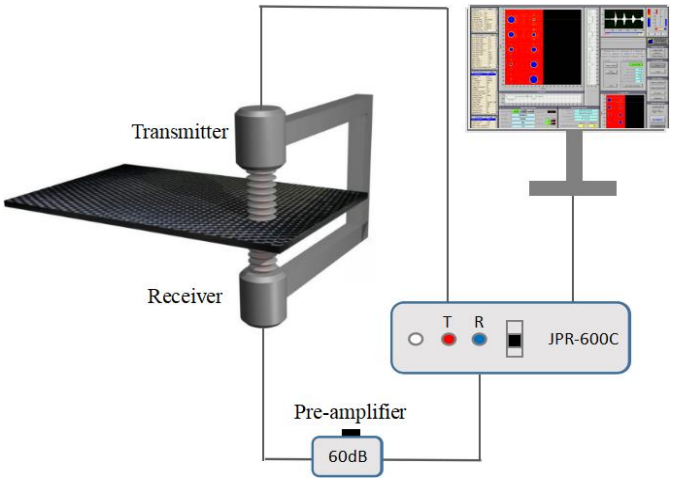

Fig.5 Air-coupled ultrasonic testing system

Table 3 The settings of Air-coupled ultrasonic testing system

Center Frequency(MHz)	Focal length(mm)	Bandwidth(kHz)	Translational Speed(mm/s)	Step size(mm)	Amplification(dB)	
					Pre-amplifier	software
0.4	38	10	10	0.3	60	20

The settings of ACUT system are shown in **Table 3**. The step size means that the distance between two adjacent sampling points. Due to the high attenuation of ultrasonic in air and the braided CFRP specimens, the received signal needs to be amplified by pre-amplifier and an integral amplifier. Usually, the final magnitude of amplification is about 80dB and the frequency of excitation signal is usually chosen below 1MHz. The closer distance between two transducers followed by an aliasing of multiple reflection signal which may cause the difficult recognition of ultrasonic direct wave. Taking these factors into consideration, for the accuracy of C-scan imaging, the frequency of excitation signal is chosen to 400kHz and the voltage amplitude of signal is set to 200V. On the basis of the thickness of the braided CFRP specimens and the focal length of transducers, the distance between two transducers is limited to 79.5mm finally.

The excitation signal is a linear chirp signal defined by Eq. 32

$$S(t) = \exp(j * 2\pi(f_0 t + \mu t^2)) \tag{32}$$

where f_0 is the initial frequency, μ is the chirp ratio which represents the rate of frequency of signal changes with time. The linear change in frequency over time can be defined as:

$$f = f_0 + \mu t \tag{33}$$

The default values for f_0 and μ are 50kHz and 1.125e10 Hz/s, respectively.

4. Results and discussion

In this section, the C-scan images and reconstructed images after 2D-VMD processing will be displayed and compared to demonstrate the validity of the proposed two-level approach for defect detection in braided CFRP. The attenuation of ultrasonic acoustical pressure in braided CFRP specimens is calculated and the relationship with the depth of defects has been established to achieve the non-contact, high-precision defect detection in CFRP structures.

4.1 Results of plain weave CFRP specimen with 1mm deep defects

4.1.1 C-scan images

The detection results of braided CFRP specimen are shown in **Fig.6**. As the attenuation of ultrasonic acoustical pressure occurs in the detection, the amplitudes of received signals and the pixels of C-scan image in the damaged area are remarkably different from the data received in the non-damaged area. The artificial defects in CFRP specimens have been marked by red circles and rectangles which denote the actual size of defects in the figures. As show in **Fig.6 (a)**, ten circular

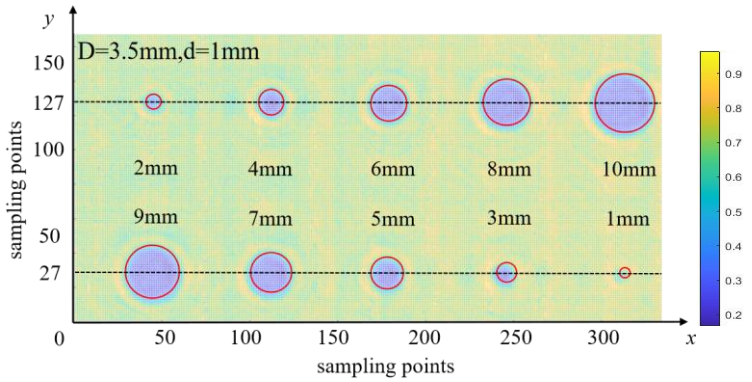

Fig.6 (a) C-scan image of plain weave CFRP specimen with 1mm deep defects

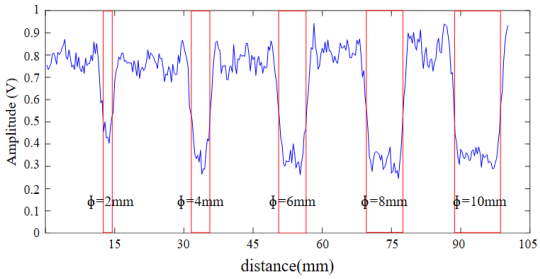

Fig.6 (b) Amplitude of upper defects signal in C-Scan image

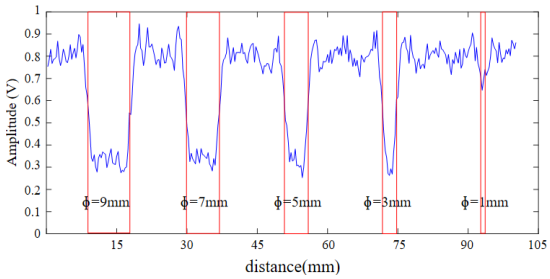

Fig.6 (c) Amplitude of lower defects signal in C-Scan image

defects with the same depth of 1mm have been conducted for detection by C-scan image and the minimum diameter which can be clearly detected is about 1~2mm. A high level of amplitudes of the receiving signal are observed in the non-damaged area. While transducers move close to the edge of artificial defects, the waveform of the ultrasonic wave is separated into two parts and travels in different thicknesses. Some ultrasonic waves traverse the defects in a thin thickness and the others traverse the CFRP specimen in a thicker normal area. Therefore, the amplitude value of received signals near the edge of defects is usually lower than that in the non-destructive area, leading to the size of detected defects larger than actual defects and the failure to detect micro size defects around the edge especially in the specimens with deep defects. When transducers move to the damaged area, the amplitude of ultrasonic waves reduces rapidly and then maintains a low level of values until reaching to another edge.

In **Fig.6 (b)** and **Fig.6 (c)**, curves representing the signals at the location of Y=27 and Y =127 have been generated by the defects at the upper and lower rows, respectively. It is noted that the amplitude of signals for the defect of diameter 1mm in **Fig. 6 (c)** is obviously higher than results generated by other defects, leading to the difficulty to differ from the signals from non-damaged areas. Except for the defects with the diameters of 1mm and 2mm, other defects have almost the same amplitude and attenuation of signals representing the acoustical pressure. It proves that the ultrasonic attenuation in defects is not primarily associated with its diameter size.

4.1.2 The processed results of 2D-VMD

Utilizing the proposed 2D-VMD technique, the images generated in C-scan process have been denoised for the improved quality of reconstruction. As shown in the **Fig.7 (a)**, it has been noted that blurs and noise in C-scan images have been effectively controlled by the 2D-VMD processing.

Owing to the original information left intact, the defects can be more easily analyzed and identified. As compared with the results in **Fig.6 (b)** and **(c)**, the amplitude of signals processed by 2D-VMD method is averagely lower than the result based on C-scan images. Therefore, the effect of the noise on the result has been reduced and the artificial defects are more easily identified with clear boundaries as shown in **Fig.7 (b)** and **Fig.7 (c)**.

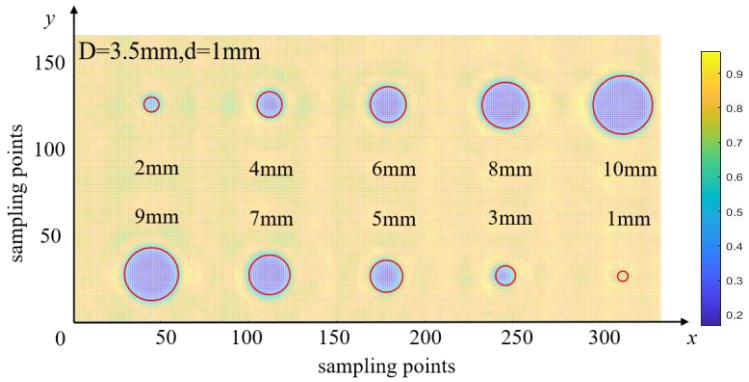

Fig.7 (a) The reconstructed image of plain weave CFRP specimen with 1mm deep defects

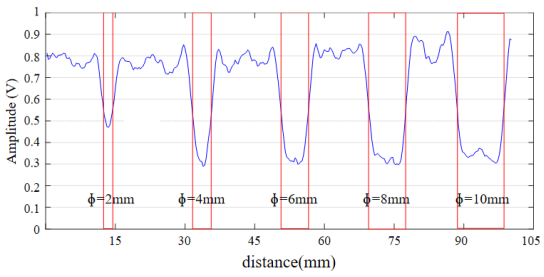

Fig.7 (b) Amplitude of defects signal in reconstructed image

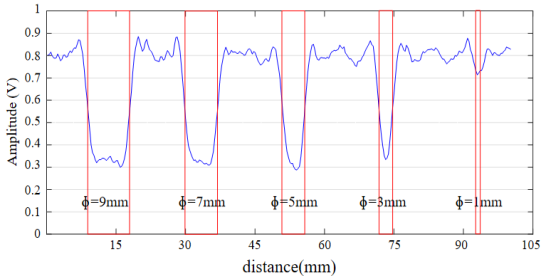

Fig.7 (c) Amplitude of defects signal in reconstructed image

4.2 Results of plain weave CFRP specimen with 2mm deep defects

4.2.1 C-scan images

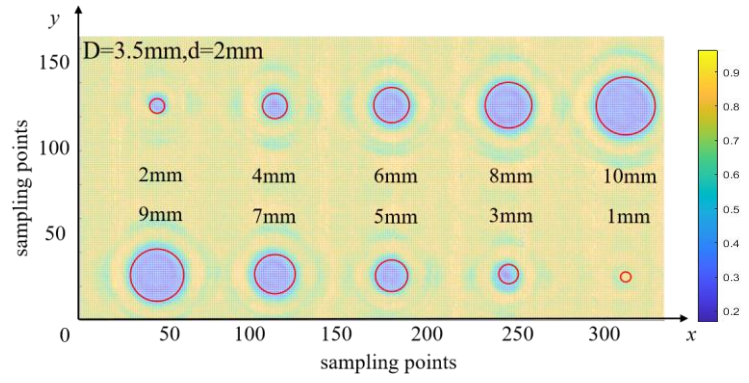

Fig.8 (a) C-scan image of plain weave CFRP specimen with 2mm deep defects

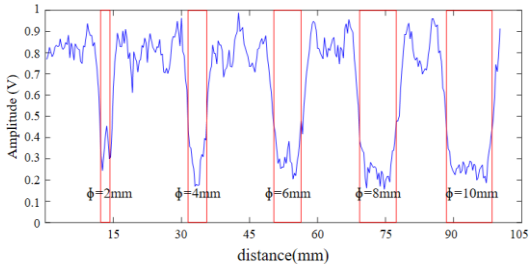

Fig.8 (b) Amplitude of upper defects signal in C-Scan image

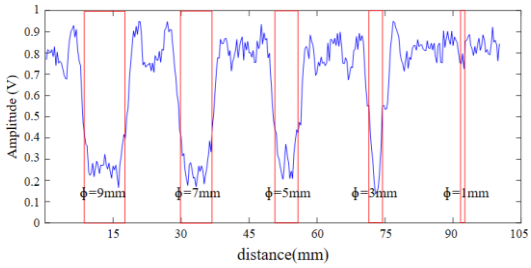

Fig.8 (c) Amplitude of lower defects signal in C-Scan image

The C-scan image for the defects with the depth of 2mm is shown in **Fig.8 (a)**, the artificial defect with the diameter of 1mm is hardly identified, while the other defects with the diameter lager than or equal to 2mm can be easily detected. As compared with the 1mm depth defects, the amplitude of signals generated by the 2mm depth defects is lower overall. Some waves are reflected and scattered when ultrasonic waves come into contact with the inner wall of defects and specimen boundary. The waveforms in different directions are superimposed, and the "shadows" representing the shape of defects are formed between adjacent defects or between defects and boundaries of the braided CFRP in the C-scan image, especially for the larger size or deeper defects. As shown in **Fig.8 (b)** and **(c)**, the manifestation of shadows in signal amplitude between adjacent defects is lower than the value of the normal areas, but much higher than that of the defected area.

4.2.2 The processed results of 2D-VMD

As shown in **Figs.9** and **10**, the C-scan image processed by 2D-VMD method indicates that the "shadows" are suppressed to a great extent, the effect of the noisy point and extremum on the reconstructed image is erased.

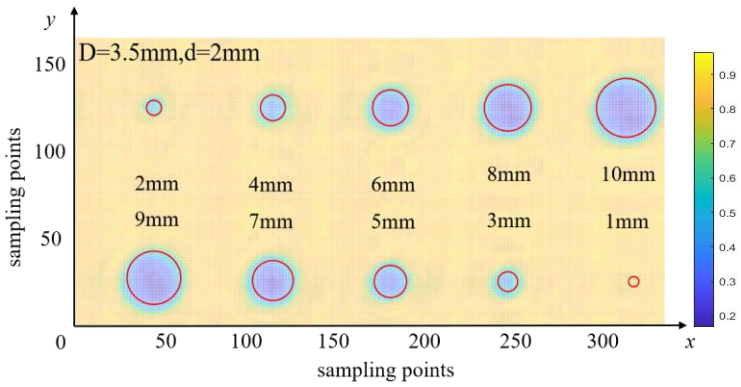

Fig.9 (a) The reconstructed image of plain weave CFRP specimen with 2mm deep defects

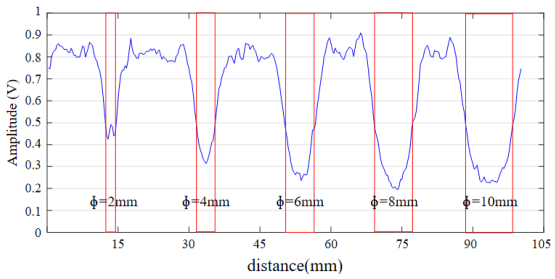

Fig.9 (b) Amplitude of upper defects signal in reconstructed image

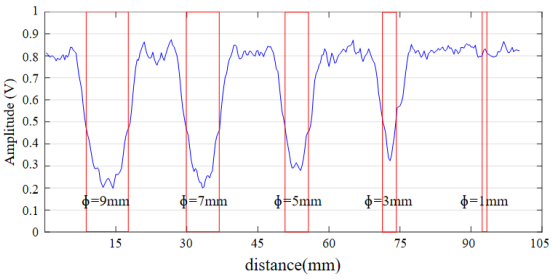

Fig.9 (c) Amplitude of lower defects signal in reconstructed image

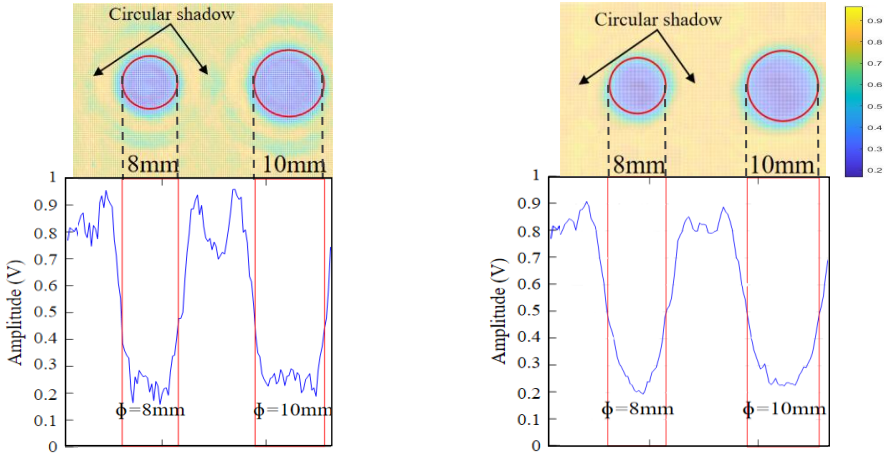

Fig.10 The comparision of shadows in C-scan and reconstructed image

Table 4 The amplitude of defect signal in C-scan image

	Amplitude of defects signal with different diameters(V)									
Diameter(mm)	1	2	3	4	5	6	7	8	9	10
d=1mm	0.7138	0.4699	0.3344	0.2896	0.2878	0.2995	0.3093	0.296	0.3	0.3045
d=2mm	0.7926	0.4246	0.3233	0.314	0.2794	0.2364	0.2047	0.1944	0.1985	0.2278

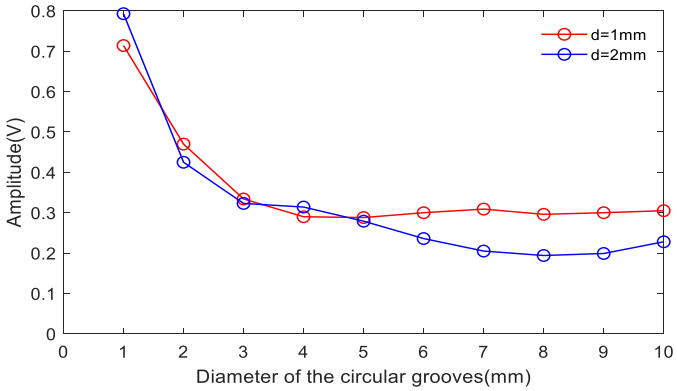

Fig.11 The amplitude of defects signal with different diameters

Table 5 The amplitude of defect signals in reconstructed image

	Amplitude of defects signal with different diameters(V)									
Diameter(mm)	1	2	3	4	5	6	7	8	9	10
d=1mm	0.638	0.364	0.263	0.235	0.25	0.245	0.257	0.235	0.24	0.234
d=2mm	0.677	0.198	0.098	0.11	0.169	0.111	0.146	0.136	0.136	0.135

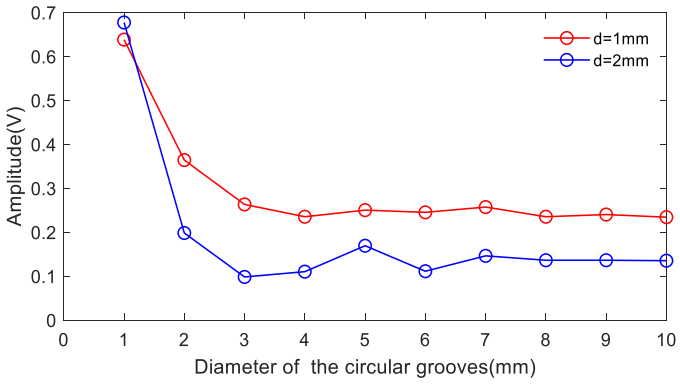

Fig.12 The amplitude of defects signal with different diameters

The amplitude of defect signal in plain weave braided CFRP specimens with 1mm and 2mm depth circular artificial defects are shown in the **Table 4** and **Fig.11**. The corresponding amplitude of defect signal after 2D-VMD processing are shown in **Table 5** and **Fig.12**. It can be observed that compared with circular artificial defects with the depth of 1mm, the ultrasonic energy attenuation is more obvious in circular artificial defects with the 2mm depth. The detailed ultrasonic acoustical pressure attenuation of these two specimens will be displayed and compared in the next section.

4.3 Results of plain weave CFRP specimen with different deep defects

Artificial defects in the braided CFRP specimen as shown in **Fig.4 (c)** have the same diameter of 8mm. **Fig.13 (a)** shows that there are still shadows around the defects and the shadows are more obvious with the increase of the defect depth. It is also noted that the noise has resulted in the inconsistent amplitude of the same defect in **Figs.13 (b)** and **(c)**. Owing to the effective denoising capability of 2D-VMD method in **Fig.14 (a)**, the side-effect of the noise and most of shadows in C-scan images disappear. As observed from the **Fig.14 (b)**, the variation of the ultrasonic acoustical pressure attenuation in circular and square artificial defects with the same depth is almost identical which proves that the ultrasonic attenuation is independent of the defect shape. With the increase of the specimen thickness, the amplitude of received signals processed by 2D-VMD method gradually decreases. However, the degree of the declination weakens.

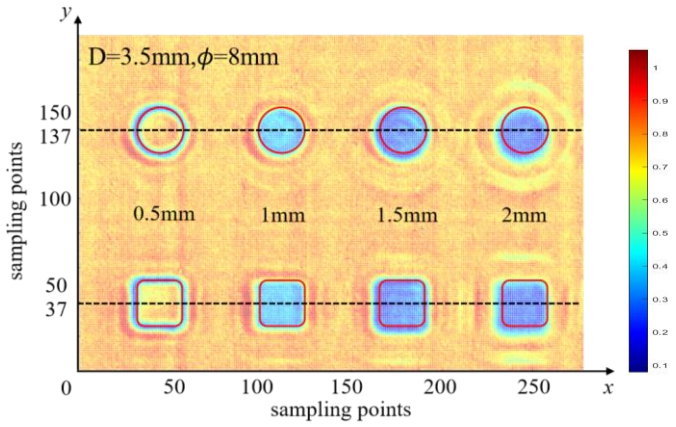

Fig.13 (a) C-scan image of plain weave CFRP specimen with different deep defects

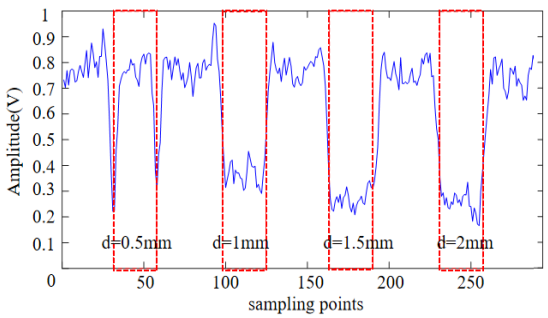

Fig.13 (b) Amplitude of circular defects signal in C-scan image

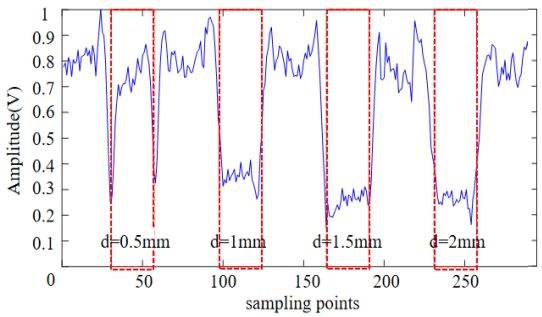

Fig.13 (c) Amplitude of square defects signal in C-scan image

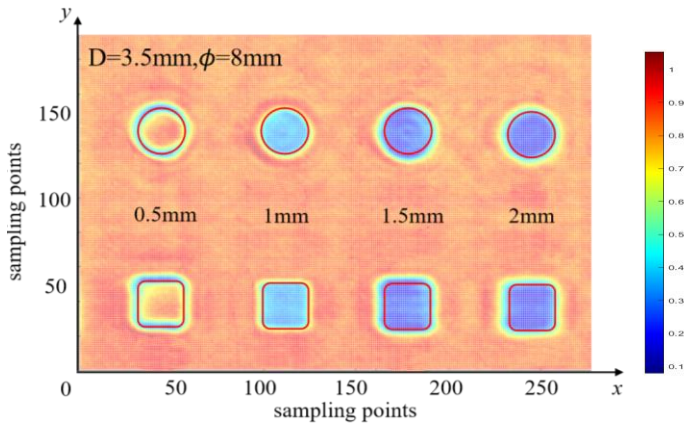

Fig.14 (a) The reconstructed image of plain weave CFRP specimen with different deep defects

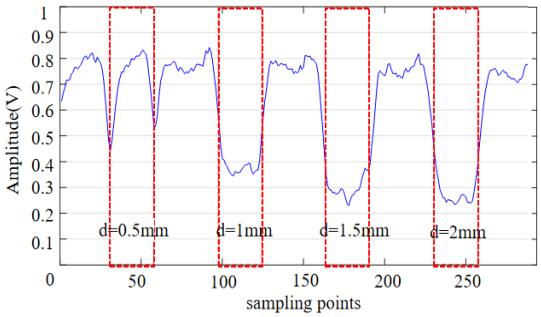

Fig.14 (b) Amplitude of circular defects in reconstructed image

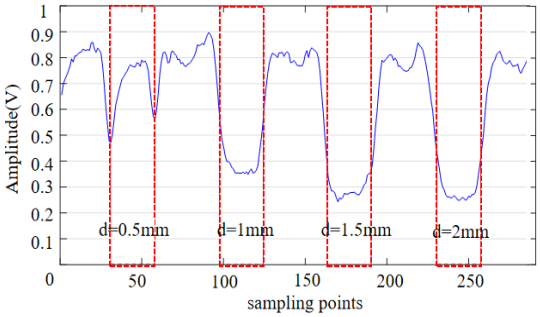

Fig.14 (c) Amplitude of square defects l in reconstructed image

Table 6 Amplitude of defects signal in plain weave CFRP specimens

Depth (mm)	Amplitude (V)							
	Case a		Case b		Case c			
					Circular defects		Square defects	
	C-scan	2D-VMD	C-scan	2D-VMD	C-scan	2D-VMD	C-scan	2D-VMD
d=0.0	0.8771	0.8725	0.8771	0.8725	0.8771	0.8725	0.8771	0.8725
d=0.5	#	#	#	#	0.708	0.4852	0.674	0.5169
d=1.0	0.271	0.348	#	#	0.28	0.3497	0.268	0.3488
d=1.5	#	#	#	#	0.179	0.2629	0.17	0.2723
d=2.0	#	#	0.18	0.237	0.182	0.2371	0.199	0.2477

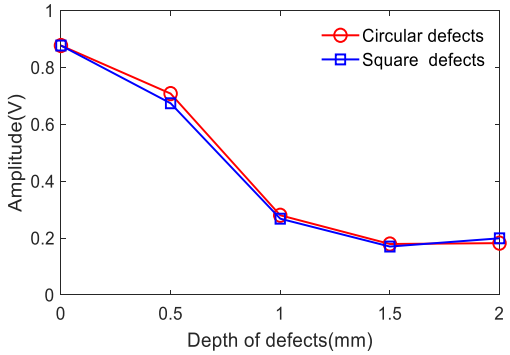

Fig.15 (a) Amplitude of receiving signal at different depth

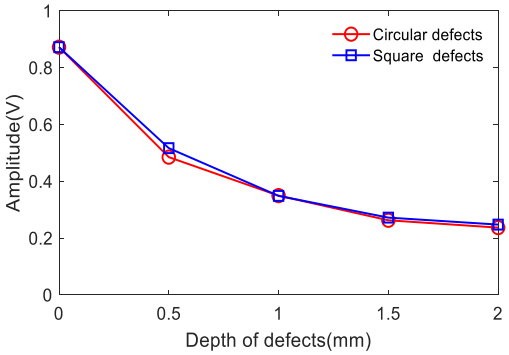

Fig.15 (b) Amplitude of processed signal at different depth

Table 7 Ultrasonic acoustical pressure attenuation of defects in plain weave CFRP specimens

Depth (mm)	Attenuation (dB)							
	Case a		Case b		Case c			
					Circular defects		Square defects	
	C-scan	2D-VMD	C-scan	2D-VMD	C-scan	2D-VMD	C-scan	2D-VMD
d=0.0	3.298	3.343	3.298	3.343	3.298	3.343	3.298	3.343
d=0.5	#	#	#	#	5.145	8.428	5.509	7.878
d=1.0	12.498	13.003	#	#	13.19	11.259	13.571	11.282
d=1.5	#	#	#	#	17.063	13.725	17.511	13.419
d=2.0	#	#	19.209	15.34	16.906	14.609	16.131	14.229

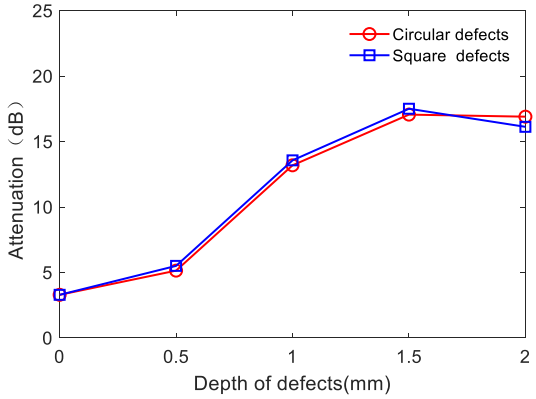

Fig.16 (a) Acoustical pressure attenuation in C-scan image

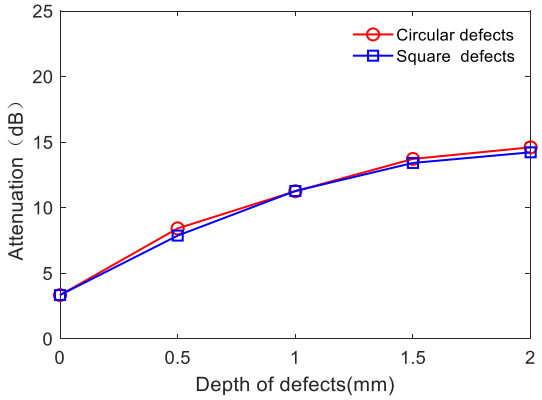

Fig.16 (b) Acoustical pressure attenuation in reconstructed image

The amplitude of received signals at different depths in plain weave braided CFRP specimens is shown in **Table 6** and **Fig.15**. As shown in **Fig.15**, the red and blue curves denote the signal amplitude of circular and square defects at different depth, respectively. Using Eq.31, the signal amplitude of defects in the third CFRP specimen is converted into the ultrasonic acoustical pressure attenuation shown in **Table 7**. The ultrasonic acoustical pressure of circular defects is almost identical to that of square defects in whatever the C-scan images or the reconstructed images. As observed in **Fig.16 (a)**, the attenuation of ultrasonic acoustical pressure changes irregularly. Employing 2D-VMD, the ultrasonic acoustical pressure attenuation of defects in the third plain weave CFRP specimen increases with the depth of artificial defects in **Fig.16 (b)**. As compared with the attenuation shown in C-scan images, results of new reconstructed images are in a good

agreement with the theoretical calculations and more reliable information about defects in the plain weave CFRP are obtained.

4.4 Results of twill weave CFRP specimen with different deep defects

The twill weave CFRP specimen as shown in **Fig4. (d)** differs from the plain weave CFRP specimens in terms of the weave type of carbon fiber. As shown in **Fig.17 (a) and (b)**, the artificial defects with the depth in the range of 0.25mm to 2mm can be clearly identified using C-scan and 2D-VMD techniques, respectively. The shadow effect of ultrasonic waves on the accuracy of detection has been analyzed between the adjacent defects, especially in the vicinity of deep defects.

As shown in **Fig.18**, the amplitudes of received signals for the defects by C-scan and 2D-VMD method have been described. The red curves denote the signal at the points whose vertical coordinate is selected as Y=145, traveling across the artificial defects from left to right. Similarly, the blue curves represent the points on the line with the vertical coordinate Y=45. As compared with the results by the C-scan detection technique, the detection quality has been remarkably improved near the vicinity of the edge using the proposed 2D-VMD method. It is noted that the noise has been successfully removed from the received signals in the detection process and this has demonstrated the proposed method with the capability of denoising.

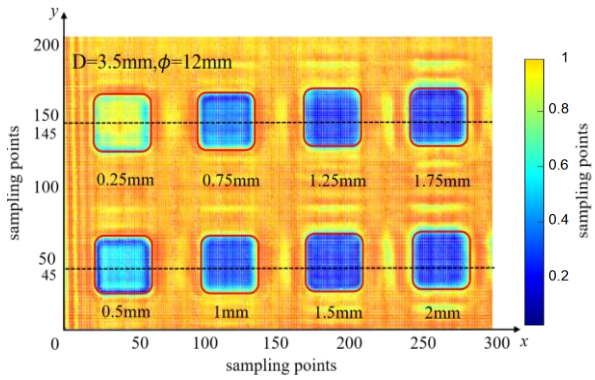

Fig.17 (a) C-scan image of twill weave CFRP specimen

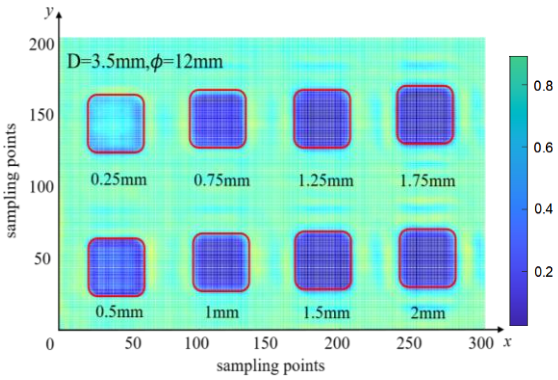

Fig.17 (b) The reconstructed image of twill weave CFRP specimen

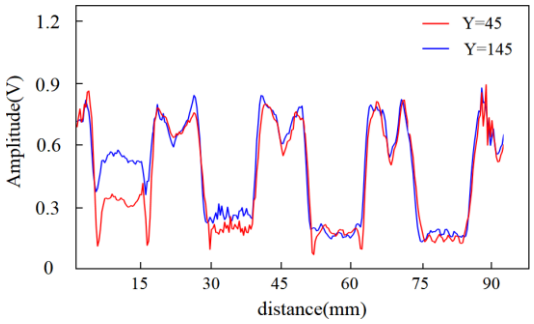

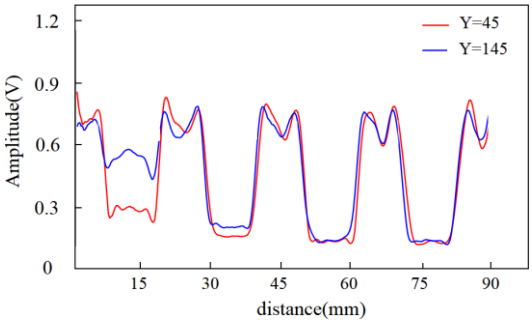

Fig.18 (a) The amplitude of defects in C-scan image

Fig. 18 (b) The amplitude of defects in reconstructed image

The calculated attenuation of ultrasonic acoustical pressure in the twill weave CFRP specimen is shown in **Table 8.** As compared with the results of plain weave CFRP specimens, the attenuation of ultrasonic acoustical pressure in twill weave CFRP specimen is obviously higher. It is worth noting that the ultrasonic acoustical pressure attenuation in undamaged areas in the twill weave CFRP is 76.61% higher than that in the plain weave CFRP. Using the proposed 2D-VMD method, the ratios of the pressure attenuation between two weave types of CFRPs for the cases with different defect depths of 0.5mm, 1mm, 1.5mm, 2mm are 73.95%, 65.26%, 48.25%, 41.04%, respectively. These results demonstrate that different weave types of braided CFRP does have a remarkable influence on the ultrasonic acoustical pressure attenuation. In general, the plain weave CFRP is more conductive to the propagation of ultrasonic waves.

The curves in **Fig.19** representing the attenuation of ultrasonic acoustical pressure have been obtained by C-scan and reconstructed image for the twill weave CFRP specimen. The attenuation gradually increases with the depth, while the gradient of the increase trends to be slight. With the depth of structural defects in the range of 0 to 2mm, the attenuation of the acoustical pressure increases up to the maximum value at the depth of 1.625mm ($d = D - \lambda/4$ and D is the plate thickness) and then declines. This helps explain that when the damage depth is deeper than 2mm, the attenuation value of ultrasonic pressure will continue to decline. When the depth is equal to 3.5*mm* (the plate thickness), the defect is a through hole and the attenuation will decline to zero. Moreover, the trend of the acoustical pressure attenuation using C-scan has seen a less smooth increase than the result in reconstructed image. The difference of acoustical pressure attenuation between the C-scan

and reconstructed images has been reduced more than that in plain weave CFRP specimens. Also, the comparison results have indicated a good agreement with each other.

Table 8 Attenuation of ultrasonic acoustical pressure in plain and twill weave CFRP

Depth (mm)	Attenuation (dB)			
	Plain weave CFRP		Twill weave CFRP	
	C-scan	2D-VMD	C-scan	2D-VMD
d= 0.0	3.298	3.343	6.243	5.904
d=0.25	#	#	9.168	8.733
d= 0.5	5.327	8.153	16.115	14.182
d=0.75	#	#	16.488	16.243
d= 1.0	13.381	11.271	18.154	18.627
d=1.25	#	#	19.243	19.956
d= 1.5	17.287	13.572	21.327	20.12
d=1.75	#	#	19.893	20.209
d= 2.0	16.519	14.419	19.954	20.336

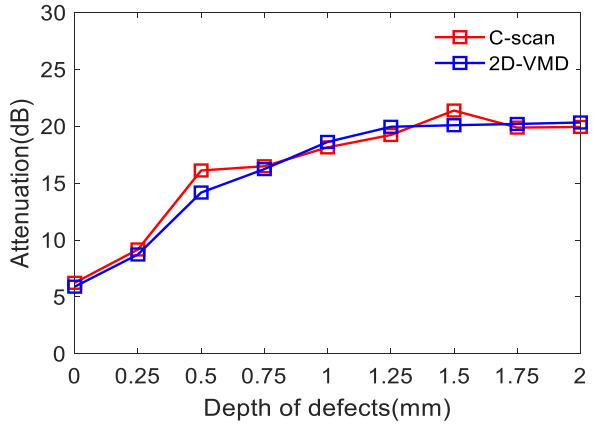

Fig.19 Ultrasonic acoustical pressure attenuation of defects in twill weave CFRP specimen

5. Conclusion

In this paper, a novel two-level defect identification approach based on 2D-VMD method has been proposed. Influences of the defect size, shape, depth and the weave type of carbon fibers in braided CFRP specimens on the ultrasonic acoustical pressure have been discussed throughout experimental tests. In the proposed two-level approach, the high-accuracy reconstruction of new images has been realized by reducing the noise, structural vibration and other disturbances in the

process of C-scan. The relationship between the defect depth and the attenuation of acoustical pressure has been established, ultimately enabling reliable identification and quantification of defects. Results have shown that the proposed method has a good capability of detecting defects with the minimum diameter of about 1~2mm. As the depth of structural defects has increased, the ultrasonic acoustical pressure attenuation has become more distinct and the change of magnitudes in attenuation has less sensitive, leading to the flatter curve in the defect area. Meanwhile, remarkable influences of the weave type of carbon fibers in braided CFRP specimens on the ultrasonic acoustical pressure attenuation have been investigated. The ultrasonic waves have been more prone to propagating in the plain weave CFRP than the twill weave CFRP. Summarily, the proposed detection method has demonstrated the great capability of eliminating the shadows around structural defects to a large extent in the reconstructed images and the excellent feasibility for the non-contact, high-precision defect detection and identification in braided CFRP structures. Considering the practical circumstances, such as the existences of the delamination, inclusions and pores in braided CFRP, there will be a discrepancy between the prediction of the acoustical pressure attenuation in the actual defect inspections and the theoretical results. Research on the establishment of accurately quantitative relationships between the ultrasonic energy attenuation and the aforementioned factors will be further carried out in the future work.

6. Acknowledgments

This work was funded by the National Natural Science Foundation of China (No. 11611530686), the State Key Laboratory of Mechanics and Control of Mechanical Structures at NUAA (MCMS-E-0520K02), and the Opening Project of Applied Mechanics and Structure Safety Key Laboratory of Sichuan Province(SZDKF-202002), and the Priority Academic Program

Development of Jiangsu Higher Education Institutions (PAPD).

References

[1] J. Peters, Non-Contact Inspection of Composites Using Air-Coupled Ultrasound, 22 (2003) 973–980.

[2] I.Y. Yang, U. Heo, K.S. Lee, J.W. Park, Y.S. Kweon, D.K. Hsu, Y.T. Cho, C.H. Lee, K.H. Im, Non-Contact and Contact Ultrasonic Detection of Fiber Orientation in Orthotropic Composite Laminates, Key Eng. Mater. 324–325 (2006) 419–422.

[3] T. Hasiotis, E. Badogiannis, N.G. Tsouvalis, Application of ultrasonic C-scan techniques for tracing defects in laminated composite materials, Stroj. Vestnik/Journal Mech. Eng. 57 (2011) 192–203.

[4] A. Quattrocchi, F. Freni, R. Montanini, Comparison between air-coupled ultrasonic testing and active thermography for defect identification in composite materials, Nondestruct. Test. Eval. 36 (2019) 97–112.

[5] O. Ahmed, X. Wang, M.V. Tran, M.Z. Ismadi, Advancements in fiber-reinforced polymer composite materials damage detection methods: Towards achieving energy-efficient SHM systems, Compos. Part B Eng. 223 (2021) 109136.

[6] A. Römmeler, P. Zolliker, J. Neuenschwander, V. van Gemmeren, M. Weder, J. Dual, Air coupled ultrasonic inspection with Lamb waves in plates showing mode conversion, Ultrasonics. 100 (2020) 105984.

[7] M.S. Harb, F.G. Yuan, Non-contact ultrasonic technique for Lamb wave characterization in composite plates, Ultrasonics. 64 (2016) 162–169.

[8] A. Poudel, S.S. Shrestha, J.S. Sandhu, T.P. Chu, C.G. Pergantis, Comparison and analysis of Acoustography with other NDE techniques for foreign object inclusion detection in graphite epoxy composites, Compos. Part B Eng. 78 (2015) 86–94.

[9] H. Jeong, D.K. Hsu, Experimental analysis of porosity-induced ultrasonic attenuation and velocity change in carbon composites, Ultrasonics. 33 (1995) 195–203.

[10] M.D. Farinas, T.E.G. Alvarez-Arenas, E.C. Aguado, M.G. Merino, Non-contact ultrasonic inspection of CFRP prepregs for aeronautical applications during lay-up fabrication, IEEE Int. Ultrason. Symp. IUS. (2013) 1590–1593.

[11] S. Biwa, Independent scattering and wave attenuation in viscoelastic composites, Mech. Mater. 33 (2001) 635–647.

[12] S.S. Ding, S.J. Jin, Z.B. Luo, J. Chen, L. Lin, Researches on the ultrasonic scattering attenuation of carbon fibre reinforced plastics with 2D real morphology void model, Acoust. Phys. 63 (2017) 490–495.

[13] Z. Tian, Y. Lingyu, C. Leckey, J. Seebo, Guided wave imaging for detection and evaluation of impact-induced delamination in composites, Smart Mater. Struct. 24 (2015) 105019.

[14] Z. Tian, L. Yu, C. Leckey, Rapid guided wave delamination detection and quantification in composites using global-local sensing, Smart Mater. Struct. 25 (2016) 1–11.

[15] R. Livings, V. Dayal, D. Barnard, Damage Detection in a Multi-Layered, Multi-Material Composite Using Air-Coupled Ultrasonic Resonance Imaging, J. Nondestruct. Eval. 35 (2016) 55-63.

[16] A. Asokkumar, E. Jasiūnienė, R. Raišutis, R.J. Kažys, Comparison of ultrasonic non-contact air-coupled techniques for characterization of impact-type defects in pultruded gfrp composites, Materials (Basel). 14 (2021) 1–25.

[17] J. Neuenschwander, R. Furrer, A. Roemmeler, Application of air-coupled ultrasonics for the characterization of polymer and polymer-matrix composite samples, Polym. Test. 56 (2016) 379–386.

[18] L. Bustamante, N. Jeyaprakash, C.H. Yang, Evaluation of Defect Detection in Aluminium, CFRP and Epoxy Resin Plates Using Non-contact Air-Coupled Ultrasonic Waves, Int. J. Precis. Eng. Manuf. 21 (2020) 1843–1856.

[19] L. Bustamante, N. Jeyaprakash, C.H. Yang, Hybrid laser and air-coupled ultrasonic defect detection of aluminium and CFRP plates by means of Lamb mode, Results Phys. 19 (2020) 103438.

[20] H. Li, Z. Zhou, Air-coupled ultrasonic signal processing method for detection Stomata defects in materials, NDT E Int. 92 (2017) 167–176.

[21] N.E. Huang, Z. Shen, S.R. Long, M.C. Wu, H.H. Snin, Q. Zheng, N.C. Yen, C.C. Tung, H.H. Liu, The empirical mode decomposition and the Hubert spectrum for nonlinear and non-stationary time series analysis, Proc. R. Soc. A Math. Phys. Eng. Sci. 454 (1998) 903–995.

[22] Y.S. Chang, Z. Yan, K.H. Wang, Y. Yao, Non-destructive testing of CFRP using pulsed thermography and multi-dimensional ensemble empirical mode decomposition, J. Taiwan Inst. Chem. Eng. 61 (2015) 54–63.

[23] K. Dragomiretskiy, D. Zosso, Variational mode decomposition, IEEE Trans. Signal Process. 62 (2014) 531–544.

[24] Y.J. Xue, J.X. Cao, D.X. Wang, H.K. Du, Y. Yao, Application of the Variational-Mode Decomposition for Seismic Time-frequency Analysis, IEEE J. Sel. Top. Appl. Earth Obs. Remote Sens. 9 (2016) 3821–3831.

[25] K. Dragomiretskiy, D. Zosso, Two-dimensional variational mode decomposition, Lect. Notes Comput. Sci. (Including Subser. Lect. Notes Artif. Intell. Lect. Notes Bioinformatics). 8932 (2015) 197–208.

[26] A.J. Zuckerwar, Atmospheric absorption of sound: Update, J. Acoust. Soc. Am. 88 (1990) 2019–2021.